J. Hydrol. Hydromech., 68, 2020, 3, 211–222
DOI: 10.2478/johh-2020-0021
ISSN 1338-4333

sciendo Journal of Hydrology and Hydromechanics

Three-dimensional numerical study of submerged spatial hydraulic jumps

Ahmed S. Foda[1*], Yehya E. Imam[1,2], Abd Allah S. Bazaraa[1], Emad H. Imam[3]

[1] Department of Irrigation and Hydraulics, Faculty of Engineering, Cairo University, Giza, Egypt.
[2] Environmental Engineering Program, University of Science and Technology, Zewail City of Science and Technology, Giza, Egypt.
[3] Department of Construction Engineering, American University in Cairo, Giza, Egypt.
[*] Corresponding author. E-mail: a.foda@tamcon-eg.com

Abstract: A three-dimensional numerical model was applied to simulate submerged spatial hydraulic jumps (SSHJ) downstream of a symmetric vent that discharges into a wider channel. Simulations were carried out for different aspect ratios of the vent, expansion ratios of vent width to downstream channel width, tailwater depth, and inlet Froude number. Depending on these factors, simulations indicated the formation of steady asymmetric SSHJ, oscillatory asymmetric SSHJ, and steady symmetric SSHJ, consistent with results of previous experimental studies. The model reproduced observed depth downstream of vent, jump length, and velocity profiles along channel centerline for steady symmetric SSHJ. For oscillatory asymmetric SSHJ, simulated oscillation frequencies had Strouhal numbers that varied with expansion ratio and ranged between 0.003 and 0.015. With piers downstream of the vent, oscillatory SSHJ continued to exhibit jet deflections when pier length was relatively short (≲0.2 of jump length) but became steady asymmetric for longer piers.

Keywords: Abrupt channel expansion; Submerged spatial hydraulic jump; Asymmetric jump; Oscillatory jump; Computational fluid dynamics.

1 INTRODUCTION

Hydraulic jumps in open channels have an important role in the dissipation of excessive energy downstream of hydraulic structures. The hydraulic jump roller dissipates the energy of supercritical flow shooting from structure vents and transforms it to less erosive subcritical flow. Depending on the location of the jump roller relative to structure vents, different types of hydraulic jumps may occur between piers separating vents and in the wider downstream channel. When the jump is formed between the piers, it is referred to as a classical jump similar to hydraulic jumps in prismatic channels (Hager, 1992). Transitional jumps are formed partly between piers and partly downstream of the piers in the wider channel. The focus of this study is the so-called spatial hydraulic jump which forms entirely in the wider channel immediately downstream of piers. In particular, we focus on the submerged spatial hydraulic jump which forms when vents are located at downstream end of piers, tailwater depth is large enough to submerge the hydraulic jump, and water depth immediately downstream of vents exceeds vent height. The case considered in this paper is when the central vent is partially opened and side vents are fully closed (Figure 1a, b).

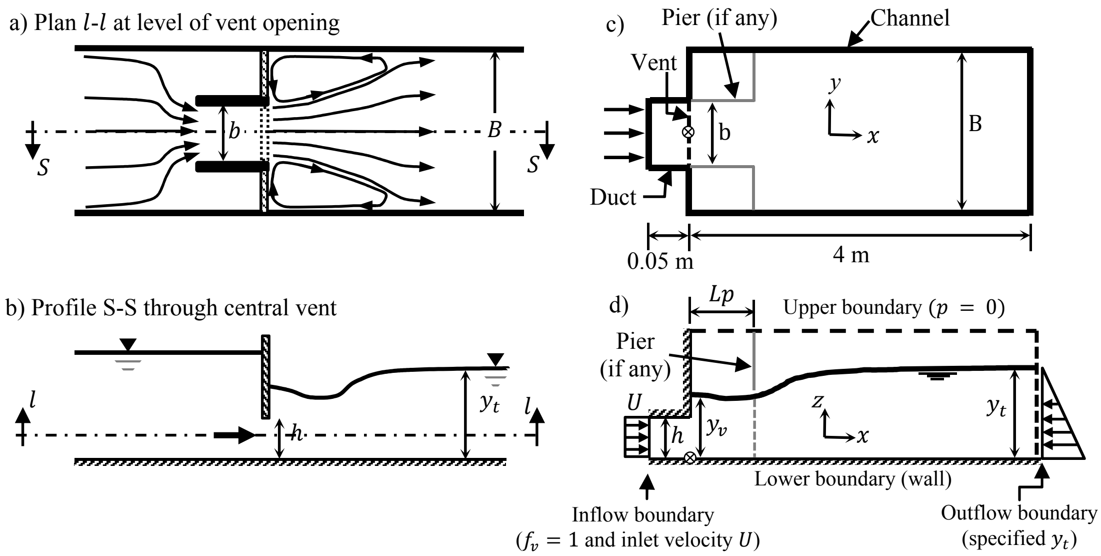

Fig. 1. a) Plan view and b) profile view S-S of a submerged spatial hydraulic jump forming downstream a multi-vent structure. Side vents are closed and only the central vent is partially opened. c) Plan view and d) profile view showing geometry and boundary conditions for the numerical mode. Also shown is the three-dimensional coordinate system x, y, and z used for presenting model results. For clarity, coordinates are shown shifted from origin which is at channel bottom at center of vent (as indicated by the ⊗ marker). Grey lines show modified geometry in simulations with downstream piers.

A number of previous experimental studies examined the submerged spatial hydraulic jump (SSHJ) at abrupt symmetric expansions in rectangular channels. Rajaratnam and Subramanya (1968) focused on the formation of stable symmetric SSHJ and did not consider asymmetric or unstable flow patterns. Rajaratnam and Subramanya (1968) indicated that the formation of stable symmetric SSHJ requires a minimum tailwater depth that depends on vent height h, vent width b, and inlet Froude number. Due to limited range of experimental parameters, Rajaratnam and Subramanya (1968) were led to conclude that the minimum tailwater depth for symmetric SSHJ was independent of channel width B downstream of the vent.

Ohtsu et al. (1999) performed a more comprehensive experimental study of SSHJ. They observed three flow patterns I, II, and III which differed in how the symmetry and steadiness of the hydraulic jump changed with tailwater depth. The formation of a particular flow pattern from among these three patterns depended on two factors: the expansion ratio $\alpha = b/B$, defined as the ratio of vent width b to channel width B, and the aspect ratio $\beta = b/h$, defined as the ratio of vent width b to vent height h (Figure 1). For flow pattern I, increase in tailwater depth y_t changed the SSHJ from steady asymmetric jump to oscillatory asymmetric jump and then to steady symmetric jump. For flow pattern II, increase in tailwater depth directly changed the SSHJ from steady asymmetric jump to steady symmetric jump. For flow pattern III, the SSHJ was always symmetric regardless of tailwater depth. Ohtsu et al. (1999) determined the hydraulic and geometric conditions required for the formation of steady symmetric SSHJ and oscillatory asymmetric SSHJ. For these jump types, Ohtsu et al. (1999) also measured the jump length and produced empirical equations giving jump length. Zare and Baddour (2007) carried out further experimental investigation of SSHJ downstream single symmetric vents. However, these authors focused only on symmetric SSHJ; no experiments were done on steady or oscillatory asymmetric jumps. Furthermore, experiments were limited to a narrow range of expansion and aspect ratios.

Previous investigations of hydraulic jump characteristics using numerical models focused on submerged classical hydraulic jumps (Demirel, 2015; Gumus et al., 2016; Javan and Eghbalzadeh, 2013; Jesudhas et al., 2017; Long et al., 1991; Ma et al., 2001). Fewer numerical studies examined free classical hydraulic jumps which are characterized by irregular, fluctuating water surface (Jesudhas et al., 2018; Jesudhas et al., 2020b; Qingchao and Drewes, 1994). Most numerical studies of hydraulic jumps employed two-dimensional models with a $k-\varepsilon$ turbulence closure scheme (Javan and Eghbalzadeh, 2013; Long et al., 1991; Ma et al., 2001; Qingchao and Drewes, 1994). Fewer numerical studies utilized three-dimensional models to examine free classical hydraulic jumps (Jesudhas et al., 2018, 2020b) and submerged classical hydraulic jumps (Demirel, 2015; Jesudhas et al., 2017). Simulated flow within classical submerged hydraulic jumps was highly three dimensional with strong interaction between mean flow and recirculation flow (Demirel, 2015). Compared to classical submerged jumps, spatial hydraulic jumps are expected to have more spatially variable velocities due to the abrupt expansion, which necessitate application of three-dimensional numerical models to properly characterize spatial jumps.

There seems to be no previous numerical investigations of spatial hydraulic jumps. An exception is the study by Jesudhas et al. (2020a) who focused on the symmetric spatial submerged hydraulic jump (SSHJ) and did not consider steady and oscillatory asymmetric SSHJs. The main objective of this study is to extend the previous numerical studies to submerged spatial hydraulic jumps (SSHJ). In particular, we aim to test the ability of available 3D numerical models to reproduce the characteristics and types observed in previous experimental studies of SSHJ. Results of this study are important for confirming the reliability of applying numerical models in the design and operation of multi-vent hydraulic structures. In addition, this study examines oscillatory SSHJ characteristics including oscillation frequency and amplitude which were not considered in previous experimental studies. The existence of piers extending downstream of the vent is an important practical case and the effect of pier length on oscillatory SSHJ was also examined in this study. It seems that this effect has only been addressed in the experimental study by Bremen and Hager (1993) who focused on free hydraulic jumps and did not consider submerged jumps. Other previous experimental studies that examined submerged jumps between piers did not consider oscillatory SSHJ (Bijankhan and Kouchakzadeh, 2015; Smith, 1989).

2 METHODS

2.1 Numerical simulations

2.1.1 Simulations without vent piers

Numerical simulations were carried out to reproduce the various types of SSHJ without vent piers (Table 1). Simulations were done for six values of the expansion ratio: $\alpha = 0.20$, 0.33, 0.50, 0.67, 0.9, and 0.95. Values of the aspect ratio were $\beta \cong$ 1.5, 5, 10, and 15. Inlet Froude number, $F_r = U/\sqrt{gh}$, ranged between 2.3 and 9.1 where U is the average flow velocity through the vent, h is vent height, and $g = 9.81$ m/s^2 is gravitational acceleration.

Simulations were carried out in horizontal rectangular channels of length 4.0 m (Figure 1c, d). Channel width was 0.2 m in simulations I-OA4, II-SS, and II-SA; 0.23 m in simulation I-SS2; and 0.4 m in remaining simulations (Table 1). These channel dimensions were the same dimensions used in the experimental setup of Ohtsu et al. (1999) and Zare and Baddour (2007). The same geometry was used to facilitate comparison of numerical results and the experimental observations. The channels had an inlet duct. The exit of the duct represented the vent where expansion to the wider channel occurred and SSHJ formed. The length of the duct was 0.05 m. In addition to the above lab-scale simulations, a numerical run I-OA9 was conducted with larger dimensions to examine scale effects on model results. For this run, the channel width was 4 m, the expansion ratio was 0.33, and the aspect ratio was 5.

2.1.2 Simulations with piers between vents

A second set of numerical simulations was performed to examine the effect of length of piers between vents on SSHJ characteristics and the transformation from SSHJ to transitional jumps (Figure 1c, d). A total of seven numerical simulations were done with different ratios of pier length L_p to jump roller length without pier L_j. The pier-length ratio for the simulations ranged between 3% and 100% (Table 2). All simulations were carried out in a rectangular channel with width $B = 0.4$ m, expansion ratio $\alpha = 0.33$, aspect ratio $\beta = 5$, Froude number $F_n = 3.0$, and tailwater depth $y_t = 0.115$ m. Without piers, the SSHJ would be oscillatory and asymmetric. The corresponding jump roller length is $L_j = 1.8$ m.

Table 1. Geometric and hydraulic parameters of numerical simulations. Parameters include channel width B, expansion ratio α, aspect ratio β, inlet Froude number F_r, and tailwater depth y_t at end of channel. Parameters also include flow pattern identified by Ohtsu et al. (1999).

Run name	Flow pattern	B (m)	$\alpha = \dfrac{b}{B}$	$\beta = \dfrac{b}{h}$	F_r	y_t (m)
I-SS1						0.15
I-SA		0.4	0.33	5.0	3.02	0.08
I-OA1						0.115
I-OA2		0.4	0.33	5.0	5.43	0.149
I-OA3		0.4	0.33	5.0	4.23	0.13
I-OA4	I	0.2	0.33	5.0	5.43	0.075
I-OA5		0.4	0.33	10	5.96	0.099
I-OA6		0.4	0.33	15	7.31	0.087
I-OA7		0.4	0.20	5.0	9.10	0.116
I-OA8		0.4	0.50	5.0	2.30	0.133
I-OA9		4.0	0.33	5	3.02	1.149
II-SS	II	0.2	0.67	4.7	2.43	0.10
II-SA						0.08
III-SS1	III	0.4	0.90	5.0	3.38	0.38
III-SS2†	III	0.4	0.95	5.0	3.38	0.40
I-SS2‡	I	0.23	0.20	1.5	2.00	0.135

† Simulation is for an expansion ratio exceeding the values examined by Ohtsu et al. (1999).
‡ Simulation corresponds to an experiment performed by Zare and Baddour (2007) with an aspect ratio less than values tested by Ohtsu et al. (1999). Flow type for this experiment was determined based on empirical relationship given by Ohtsu et al. (1999).

Table 2. Numerical simulations with downstream piers. Parameters shown are the pier length ratio (L_p/L_j) and pier length (L_p).

Run name	L_p/L_j (%)	L_p (m)
I-P1	3	0.05
I-P2	5	0.09
I-P3	10	0.18
I-P4	20	0.36
I-P5	50	0.91
I-P6	70	1.27
I-P7	100	1.81

2.1.3 Numerical model

The numerical model ANSYS-FLUENT 14.5 (ANSYS Inc. 2014) was used for the simulation of the three-dimensional turbulent flow within SSHJ. Simulations were based on the incompressible continuity equation and Reynolds-averaged Navier–Stokes (RANS) equations. The two-equation $k-\varepsilon$ turbulence closure parameterization was used to compute turbulent stresses; this parameterization provides reliable turbulence closure for flow through hydraulic control structures (Akoz et al., 2009). While applied boundary conditions were steady as will be shown below, unsteady terms in the continuity and RANS equations were retained to allow simulation of oscillatory flow. If unsteady terms were neglected, the model would fail to capture fluctuations associated with the oscillatory SSHJ.

Numerical solution of the governing equations in ANSYS was done using the finite volume method. A numerical grid was generated using GAMBIT 2.4.6. Because domain boundaries were straight and perpendicular, cubic elements were used in the numerical grid. The computational grid quality was high; the orthogonal index was almost unity indicating a highly orthogonal grid with expected high accuracy of numerical solution (Shaari and Awang, 2015). The numerical solution was obtained using the explicit solver in FLUENT. To ensure stability of the numerical solution, the computational time step was controlled by the Courant number which was set to unity in all numerical simulations in this study.

Because of the existence of a free water surface, numerical simulations were done as two-phase flows, namely water flow with air on top. To simulate the location and shape of water surface, the volume of fluid (VoF) method was used. This method efficiently simulates the free surface when the surface does not significantly curl on itself (Demirel, 2015; Helmi et al., 2019; Nguyen and Nestmann, 2004). For application of the VoF method, the model tracked emptying and filling of grid cells using a volume fraction f_v for each grid cell (Hirt and Nichols, 1981). Values of the volume fraction f_v ranged between 0 and 1 with $f_v = 0$ for empty cells and $f_v = 1$ for cells completely filled with water. Values of f_v between 0 and 1 indicated a partial fill with the free surface located within the grid cell.

2.1.4 Boundary conditions

At the vent inlet, uniform longitudinal velocity was applied over the vent cross-section and the vertical velocity component was set to zero (Figure 1d). The volume of fluid for inlet flow was set to unity ($f_v = 1$) to specify that the entire inflow is water in liquid phase. At the outlet of the channel, water surface was kept at a constant level corresponding to target tailwater depth and pressure distribution was assumed to be hydrostatic as the flow becomes fully developed at the downstream end of the channel. Channel sides and bottom were defined as wall boundaries with zero perpendicular velocity. No-slip condition was also applied at the wall boundaries to impose zero tangential velocity. The effect of wall roughness on near-wall flow was modeled using the law-of-wall with a roughness height of 0.15 mm for channel bed and 0.03 mm for channel sides. These roughness heights correspond to the material used in the experiments of Ohtsu et al. (1999) and Zare and Baddour (2007). Atmospheric pressure was specified at the top of the domain which was selected at a height of 0.3 m above channel bed. This height is about double the maximum water depth in the numerical simulations and ensures boundary conditions at top of domain do not affect water flow simulated in the channel.

2.1.5 Mesh resolution

Three computational grids were used to test sensitivity of model results to numerical discretization. Nominal sizes for the three grids were $d_1 = 10$ mm, $d_2 = 8$ mm, and $d_3 = 6$ mm and are referred to hereafter as coarse, medium, and fine grid resolutions, respectively. To select optimal resolution and ensure it has minimal effect on model results, the grid convergence index (GCI) that was proposed by (Roache, 1998) was used to quantify the discretization uncertainty of the numerical results. GCI was calculated using a matlab code based on the numerical solution at ~50,000 computational nodes. The calculated GCI revealed that the maximum discretization uncertainty for the medium grid results relative to the fine grid was only 1.2%. This small GCI indicated that model results for the medium grid are reliable and independent of numerical grid resolution. Because the medium-resolution grid gives reliable results and has much shorter runtime than the fine-grid resolution, the medium grid resolution of 8 mm was used as the nominal grid size for all simulations presented in the results section. When needed, smaller grid cells were used near the inlet vent. The smallest grid cell was 3 mm when the vent height was 9 mm (run I-OA6).

2.2 Model validation

Results of the numerical model was validated by comparing model results with experimental observations from Ohtsu et al. (1999) and Zare and Baddour (2007). Comparison included jump type, water depth at vent, jump length, and flow velocity distribution.

First, the simulated SSHJ type was qualitatively compared with the types identified in previous experiments, namely steady symmetric, steady asymmetric, or oscillatory asymmetric jump. The simulation of steady symmetric SSHJ was also compared against the condition specified by Rajaratnam and Subramanya (1968) for formation of this type of jump. This condition gives the minimum tailwater depth for steady symmetric SSHJ and can be recast as,

$$y_t = h\left(\frac{\beta}{2+\beta}\right)\left\{1.08 F_r \sqrt{1+\frac{2}{\beta}} + 1.4\right\} \tag{1}$$

which gives y_t as a function of vent height h, aspect ratio β, and inlet Froude number F_r.

In addition to the visual inspection of the SSHJ type, a degree of symmetry index (DSI) was used to assess the magnitude of symmetry for the distribution of the longitudinal velocity component across channel cross section. To properly assess the magnitude of symmetry, DSI was calculated over the roller length of the jump and not over the entire channel length. The degree of symmetry index was calculated using,

$$DSI = \left(1 - \frac{\sqrt{\frac{1}{n}\sum\left(u_{left} - u_{right}\right)^2}}{U}\right) \times 100\% \tag{2}$$

where u_{left} and u_{right} represent the longitudinal velocity component left and right of the longitudinal channel axis, respectively, and U is the magnitude of inlet velocity.

Besides comparing jump type, the average simulated water depth just downstream the vent was compared to the average observed water depth given by Ohtsu et al. (1999). The average simulated depth was computed based on the mean of depths at 25 to 50 computational nodes depending on channel width. The average observed depth from Ohtsu et al. (1999) was based on measurements of water depth at five locations evenly-distributed along the channel cross section immediately downstream of the vent.

In addition to comparing SSHJ type and water depth, the simulated SSHJ length was compared to experimental data. Simulated jump length was set to the length of the jump roller taken as the distance from the vent to where longitudinal flow velocity reversed from upstream direction to downstream direction. Observed jump length was obtained from Ohtsu et al. (1999) who provided empirical formulas giving jump length for all SSHJ types except the steady asymmetric type. For flow patterns I and III, the empirical formulas gave the jump length as a function of the head loss H_l in the SSHJ and the total head H_o at the inlet vent. For the symmetric jump in flow pattern II, the empirical formula for jump length was based on H_l, H_o, and also the expansion ratio α. Ohtsu et al. (1999) did not provide information about the length of the asymmetric SSHJ in flow type I.

Finally, the simulated longitudinal velocity distribution for run I-SS2 was compared to velocities measured by Zare and Baddour (2007). The comparison between simulated and measured velocities was carried out for two longitudinal profiles along the channel. The first profile was along the channel centerline and the second profile was along $y/B = 0.25$. For each profile, comparison was performed at six stations at longitudinal distance $x/y_t = 2$, 3, 4, 5, 6, and 6.5. Comparison to measured velocities was limited to the top ~92% of water depth; Zare and Baddour (2007) did not collect velocity measurements near channel bed.

Comparison between simulated and measured velocities was based on the Nash–Sutcliffe model efficiency coefficient (NSE) defined as,

$$NSE = 1 - \frac{\sum\left(u_o - u_s\right)^2}{\sum\left(u_o - \overline{u_o}\right)^2} \tag{3}$$

where u_o is observed velocity at given location and depth, u_s is corresponding simulated velocity, and $\overline{u_o}$ is average velocity. Low NSE values indicate that the average of observed velocities is a better predictor than simulated velocities. High NSE values approaching 1.0 indicates perfect agreement between simulated and observed velocities.

Besides calculating NSE, the height from channel bed to location of maximum simulated forward velocity u_m was determined for each of the locations mentioned above. This height to maximum velocity was compared to heights observed by Rajaratnam and Subramanya (1968). Observed values for δ correspond to 20% of the height from channel bed to the location where velocity $u = u_m/2$ (Rajaratnam and Subramanya, 1968).

2.3 Analysis of oscillatory SSHJ characteristics

Numerical simulations were carried out using different values of geometric and dynamical parameters to examine the characteristics of oscillatory SSHJ (Table 1). Simulations were done for three values of the expansion ratio, namely $\alpha = 0.20$, 0.33, and 0.50. Values of the aspect ratio were $\beta \cong 5$, 10, and 15. Inlet Froude number F_r ranged between 2.3 and 9.1. Tailwater depth to vent height ratio $Y_t = y_t/h$ ranged between 3.4 and 9.7.

To determine the dominant frequency of oscillations, spectral analysis was applied to simulated longitudinal velocity at two computational nodes inside the SSHJ. The two nodes were at a height 2 cm from the bed. One of the nodes was at the channel centerline and the other node was 2 cm away from the channel wall. Spectral analysis was also done for the static pressure as proxy of water depth at the two computational nodes. The relationship between velocity and water depth was examined by determining their spectral coherence and phase shift.

To identify the factors that affect the frequency of SSHJ oscillations, dimensionless analysis was applied to the following set of variables: oscillation frequency f, velocity U through inlet vent, vent height h, vent width b, channel width B, tailwater depth y_t, kinematic viscosity of water ν, and gravitational acceleration g. The outcome of dimensionless analysis was the relationship,

$$S_t = \phi\left(\alpha, \beta, F_r, R_e, Y_t\right) \tag{4}$$

where $S_t = fb/U$ is Strouhal number, $R_e = Ub/\nu$ is Reynolds number at the inlet vent, and $Y_t = y_t/h$ is the ratio of tailwater depth to the vent height. The functional dependence ϕ of S_t on the other variables in Equation (4) was tested using numerical simulations. Each of the parameters α, β, F_r, R_e, and Y_t were changed while maintaining the remaining parameters and the corresponding values of Strouhal number S_t were examined.

3 RESULTS AND DISCUSSION

3.1 Steady SSHJ

3.1.1 Symmetric versus asymmetric SSHJs

Comparison of model results and experimental observations indicated that the model reproduced the different types of SSHJ identified by Ohtsu et al. (1999). For $\beta = 5.0$, $\alpha = 1/3$, and $F_r = 3.0$, model results for run I-OA1 with the tailwater-depth ratio $y_t/h = 4.3$ indicated the formation of an unsteady asymmetric jump that will be described in detail in section 3.2. For the same β, α, and F_r, the model produced a steady symmetric jump for the relatively large tailwater-depth ratio of 5.7 in run I-SS1 and produced a steady asymmetric jump for the smaller tailwater-depth ratio $y_t/h = 3.0$ in run I-SA (Figure 2). In run I-SS1, longitudinal flow velocity was symmetrically distributed about the channel centerline and the jet flowing out of the vent did not deflect to either side of the channel (Figure 2a). Rollers were formed on both sides of the jet and had similar extents as observed by Ohtsu et al. (1999).

In run I-SA, longitudinal flow velocity was asymmetrically distributed about the channel centerline and the jet flowing out of the vent deflected to one side of the channel. The deflected jet induced rollers on both sides of the channel. The rollers had different sizes with one roller being ~6 times longer and ~2.5 times wider than the other roller (Figure 2b). The larger roller formed on the channel side opposite to the side to which the jet deflected.

For a higher $\alpha = 2/3$ and with relatively small changes in aspect ratio and inlet Froude number ($\beta = 4.7$ and $F_r = 2.4$), the model produced a steady symmetric jump for the tailwater-depth ratio $y_t/h = 3.9$ in run II-SS and a steady asymmetric jump for the smaller tailwater-depth ratio $y_t/h = 2.8$ in run II-SA (Figure 2). Similar to Ohtsu et al. (1999), longitudinal flow velocity in run II-SS was symmetrically distributed about the channel centerline, the jet flowing out of the vent did not deflect to either side of the channel, and rollers on both sides of the jet had similar extents (Figure 2c). In run II-SA, longitudinal flow velocity was asymmetrically distributed about the channel centerline and the jet flowing out of the vent deflected to one side of the channel with no oscillatory behavior, which is consistent with the observations by Ohtsu et al. (1999) (Figure 2d).

With further increase in expansion ratio from $\alpha = 2/3$ to 0.9 and with $\beta = 5.0$, $F_r = 3.4$, and tailwater-depth ratio $y_t/h = 5.3$, simulation III-SS1 produced a slightly asymmetric SSHJ. At a location 1.5 m downstream of the inlet vent, water depth was tilted with a slope of ~2% across the channel with water at the surface moving laterally from the deeper side of the channel towards the shallower side (Figure 3a). Near the channel bed, an opposite lateral current moved water from the shallower side towards the deeper side. For the α, β, and F_r parameters of run III-SS1, Ohtsu et al. (1999) gave a minimum tailwater depth ratio $y_t/h = 4.2$ for formation of symmetric SSHJ. While the ratio $y_t/h = 5.3$ imposed in run III-SS1 is higher than the

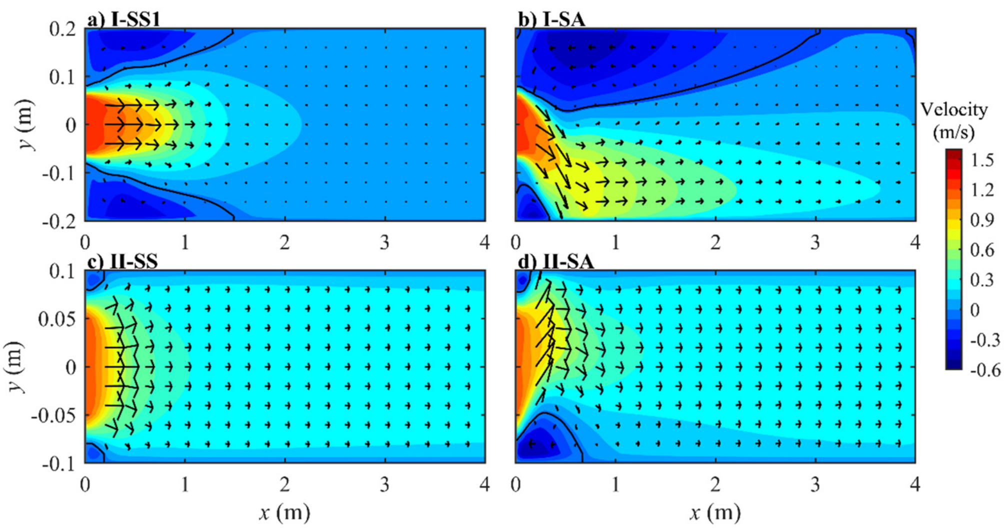

Fig. 2. Distribution of longitudinal velocity over horizontal plane at height $z = 0.02$ m above bed for a) run I-SS1, b) run I-SA, c) run II-SS and d) run II-SA. Arrows denote horizontal velocity vectors. Parameters common to runs I-SS1 and I-SA were $F_r = 3.0$, $\alpha = 1/3$, and $\beta = 5.0$. Parameters common to runs II-SS and II-SA were $Fr = 2.4$, $\alpha = 2/3$, and $\beta = 4.7$. Tailwater-depth ratio y_t/h was 5.7 for run I-SS1, 3.0 for run I-SA, 3.9 for run II-SS, and 2.8 for run II-SA. Note that the scale for the plots is distorted; longitudinal scale is smaller than lateral scale. Also, channel width is different between runs (0.4 m in runs I-SS1 and I-SA versus 0.2 m in runs II-SS and II-SA).

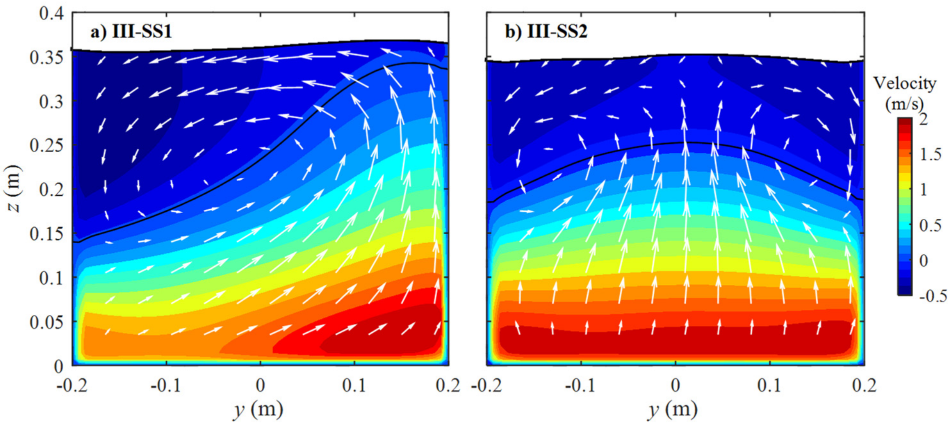

Fig. 3. Distribution of longitudinal velocity over cross section at distance $x = 1.5$ m from inlet for a) Run III-SS1 and b) Run III-SS2. Arrows denote horizontal velocity vectors. Parameters common to both runs were $Fr = 3.4$, $\beta = 5.0$, and $y_t/h = 5.3$. Expansion ratio α was 0.9 for run III-SS1 and 0.95 for run III-SS2.

minimum ratio for symmetry, run III-SS1 revealed a slightly asymmetric SSHJ pattern. This slight asymmetry was probably undetected and was neglected by Ohtsu et al. (1999) who did not measure velocity. For the same β, F_r, and y_t/h, further increase in expansion ratio α to 0.95, produces a symmetric SSHJ which is consistent with the conclusions of Ohtsu et al. (1999). Compared to run III-SS1 with $\alpha = 0.90$, run III-SS2 with $\alpha = 0.95$ revealed that water depth and velocity was symmetrically distributed about the channel centerline (Figure 3b).

Considering all simulations without oscillatory flow, the degree of symmetry index (DSI) based on longitudinal velocity ranged between 69% and 100%. The lowest DSI values of ~70% were for runs I-SA and II-SA which simulated steady asymmetric SSHJ. The highest DSI values of ~100% were for steady symmetric SSHJ simulated in runs I-SS1, I-SS2, II-SS, and III-SS2. For run III-SS1, DSI was lower amounting to 87%. Although this run simulates conditions classified by Ohtsu et al. (1999) as steady symmetric SSHJ, the simulated velocity distribution is asymmetric about the longitudinal axis of the channel leading to a relatively low DSI (Figure 3a).

3.1.2 Depth at vent

Simulated average water depth immediately downstream of the vent was in good agreement with average depth observed by Ohtsu et al. (1999). Except for run II-SA, differences between simulated and observed average depth were less than 8%. For run II-SA, the difference was significantly higher amounting to 32%. This discrepancy between simulated and observed average depth is likely due to the abrupt changes in water depth in run II-SA (not shown) and the limited number of measurements that Ohtsu et al. (1999) used to compute the average depth. Ohtsu et al. (1999) used five measurements while the simulated average depth was based on depth values at 25 computational nodes over the channel cross-section.

For runs that simulated symmetric SSHJ, model results indicated little variation in water depth across the channel width. An example is run I-SS1 which shows nearly symmetric distribution of water depth, longitudinal velocity, and resultant of transversal and vertical velocity components (Figure 4a–c). Similar to run I-SS1, water depth at the vent in runs I-SS2 and II-SS varied by up to only ~0.5% of the average depth. In run III-SS2, water depth variability was slightly higher amounting to ~4% of the average depth at the vent.

For runs that simulated asymmetric SSHJ, model results indicated greater cross-channel variability in water depth. Run I-SA is an example. For this run, water depth varied by 42% of average depth over a channel section at $x = 0.1$ m from the vent (Figure 4d). Further downstream, the jet issuing from the vent deflected towards channel side, the velocity distribution became asymmetrically distributed over the channel cross-section, and water depth variability decreased (Figure 4e, f). Water depth varied by 18% of average depth at cross-section $x = 0.3$ m and by only 3% of average depth at cross-section $x = 0.7$ m. Water surface variability was absent beyond 2 m from the vent corresponding to a distance of 26 times the tailwater depth. Compared to run I-SA, asymmetric SSHJ in runs II-SA and III-SS1 had lower cross-channel variability in water depth immediately downstream of the vent; depth variability was ~20% of average depth for runs II-SA and III-SS1, almost half the variability observed in run I-SA.

3.1.3 Velocity distribution

Simulated velocity profiles for run I-SS2 were qualitatively similar to velocity profiles along the axes of classical hydraulic jumps in prismatic channels (Figure 5) (Hager, 1992). Velocity profiles for the symmetric SSHJ in run I-SS2 indicate that maximum velocity u_m occurred at the top of the boundary layer above the channel bed. Higher in the water column, velocity decreased and then reversed from forward direction to upstream direction. With downstream distance along the channel axis, the boundary layer thickness increased and the maximum velocity decreased. The simulated boundary layer thickness and its growth were in good agreement with observations by Rajaratnam and Subramanya (1968) (Figure 5a–f). The decrease of simulated maximum velocity along the channel axis was exponential similar to the pattern observed for classical jumps (Hager, 1992). In particular, the variation of maximum velocity along the channel is well described by the empirical formula proposed by Ohtsu et al. (1990) for classical submerged jumps,

$$u_m = V_t + (V - V_t)\exp\left(-2.5\left(x / L_j\right)^{1.5}\right) \tag{5}$$

in which V_t is the cross-section average velocity at tailwater. The linear correlation coefficient between simulated u_m and values from the empirical formula is high amounting to 0.997. Furthermore, the root mean square deviation between simulated u_m and u_m from the empirical formula is only ~4% of the inlet velocity $V = 1.1$ m/s.

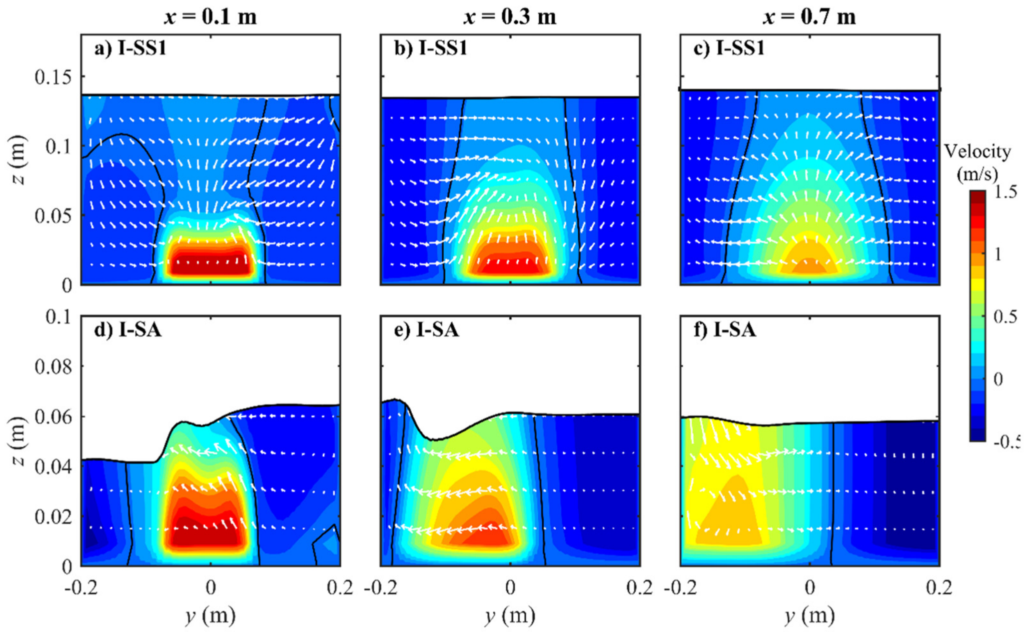

Fig. 4. Across-channel water surface for runs I-SS1 (upper panels) and I-SA (lower panels). Cross-sections are at $x = 0.1$ m (a, d), $x = 0.3$ m (b, e), and $x = 0.7$ m (c, f). Color shading shows distribution of longitudinal velocity over cross section. Arrows denote resultant of transversal and vertical velocity components. Parameters common to both runs were $\alpha = 1/3$, $\beta = 5.0$, and $F_r = 3.0$. Tailwater-depth ratio y_t/h was 5.7 for run I-SS1 and 3.0 for run I-SA.

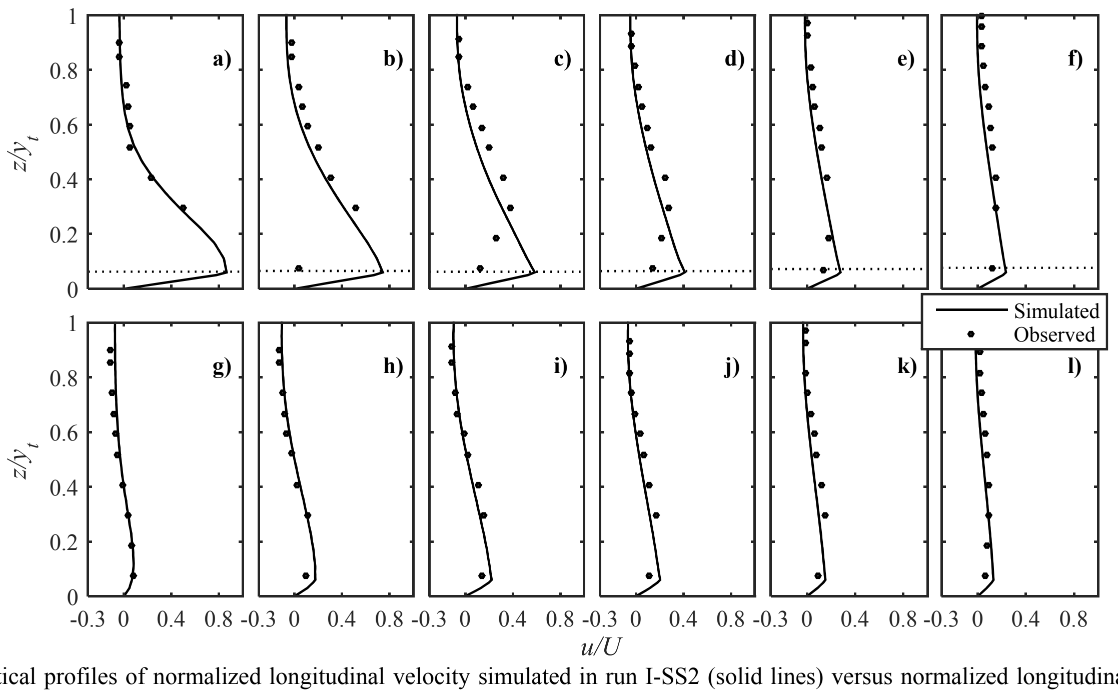

Fig. 5. Vertical profiles of normalized longitudinal velocity simulated in run I-SS2 (solid lines) versus normalized longitudinal velocities observed by Zare and Baddour (2007) (circular markers). Top panels show profiles along the channel centreline. Bottom panels show profiles along an axis midway between the channel centreline and channel wall. Horizontal dotted lines in upper panels indicate location of maximum velocity by Rajaratnam and Subramanya (1968).

Comparison of simulated velocities to corresponding observed velocities shown in Figure 5 gives a low Nash Sutcliffe model efficiency (NSE) coefficient. This low NSE is mainly due to discrepancy between simulated and observed velocities near the channel bed. If the observation nearest to the bed in each profile is excluded from comparison to simulated velocities, a much higher NSE value of 0.84 is obtained. This high NSE approaching unity indicates that the model provides reliable estimates of velocity profiles within symmetric submerged spatial hydraulic jumps and likely gives reasonable velocity estimates for asymmetric SSHJ.

For velocity near the channel bed, the model reproduced the correct thickness of the boundary layer as explained earlier. The discrepancy between simulated and observed velocities near the channel bed is likely due to atypical near-bed velocity measurements by Zare and Baddour (2007). These measurements indicate that the height to maximum velocity was considerably large amounting to four times the heights observed by

Rajaratnam and Subramanya (1968) (Figure 5c, d). The atypical near-bed velocity measurements by Zare and Baddour (2007) may be due to using an excessively rough channel bed in the experiments, an upward deflection of the jet by tilted inlet duct, or accuracy of velocity measurements being adversely affected by proximity to channel bed.

3.1.4 Jump length and energy dissipation

For symmetric SSHJ simulated in runs I-SS1, I-SS2, II-SS, and III-SS2 and slightly asymmetric SSHJ simulated in run III-SS1, the maximum length of rollers on the sides of the jet issuing from the vent ranged between 0.55 m and 2.24 m. For these SSHJs, the ratio of roller length to energy head loss L_j/H_l ranged between ~8.5 and ~19.6. The lowest ratio $L_j/H_l \approx 8.5$ was for run III-SS1 with highest expansion ratio $\alpha = 0.95$. The highest ratio $L_j/H_l \approx 19.6$ was for run I-SS2 with lowest expansion ratio $\alpha = 0.20$. For the same ratio of head loss to initial head (H_l/H_o), comparison of simulated L_j/H_l ratios to ratios calculated from the empirical formulas by Ohtsu et al. (1999) indicated good agreement (Figure 6a). For run I-SS2 with $H_l/H_o = 0.29$, there was nearly no difference between simulated and empirical L_j/H_l. There was also little difference (~2%) between simulated and empirical L_j/H_l for run III-SS2 with $H_l/H_o = 0.38$. For runs I-SS1, II-SS1, and III-SS1, deviations between simulated and empirical L_j/H_l ratios were higher ranging between 11% and 18%. However, these deviations were still less than the maximum error of 20% indicated by Ohtsu et al. (1999) for their empirical formulas. The similarity between simulated and empirical L_j/H_l ratios indicates that the model reliably reproduces the extents of symmetric SSHJs.

For steady asymmetric SSHJs in runs I-SA and II-SA, L_j/H_l ratios were higher than corresponding values for symmetric SSHJs with similar head loss ratios H_l/H_o. The asymmetric SSHJ in run I-SA had a jump length ratio $L_j/H_l \approx 36$ higher by more than fourfold compared to symmetric SSHJ with the same $H_l/H_o = 0.52$. Similarly, the asymmetric SSHJ in run II-SA had a jump length ratio $L_j/H_l \approx 17$ higher by ~20% than L_j/H_l for symmetric SSHJ with the same $H_l/H_o = 0.31$. While Ohtsu et al. (1999) did not provide jump length measurements for asymmetric SSHJs that can be used for quantitative assessment of simulated lengths for these jumps, the model results above are consistent with the qualitative observation by Ohtsu et al. (1999) about the non-compactness of asymmetric SSHJs.

3.2 Oscillatory SSHJ

3.2.1 Jet deflection pattern

Runs I-OA1 to I-OA8 revealed the occurrence of oscillatory SSHJ where the jet issuing from the vent periodically deflected between channel sides (Figure 7). In run I-OAI with $\alpha = 1/3$, $\beta = 5.0$, $F_r = 3.0$, and tailwater depth ratio $y_t/h \approx 4.3$, the jet deflected from the channel right side to the center of the channel within ~2.8 s (Figure 7a, b). The jet continued its deflection and reached the left side of the channel after another ~2.8 s (Figure 7c). The jet then reversed its deflection from the left side to the right side reaching the right wall within about ~5.7 s (not shown). The cycle of jet deflection shown in Figure 7a–c started again and the jet repeated its oscillatory deflections with a constant period of approximately 11.3 s. Similar to run I-OA1, model results for run I-OA8 revealed the occurrence of oscillatory SSHJ (Figure 7d–f). However, the SSHJ in run I-OA8 with similar $\beta = 5.0$, greater $\alpha = 0.5$, slightly smaller $F_r = 2.3$, and smaller tailwater depth ratio $y_t/h = 3.4$ had less pronounced jet oscillations and a shorter oscillation period of ~9.1 s compared to the SSHJ in run I-OA1.

The oscillatory behavior of the SSHJs that were simulated in runs I-OA1 to I-OA8 is consistent with the observations and empirical formulas of Ohtsu et al. (1999). For example, run I-OA1 reproduced the oscillatory jet deflections observed in an experiment by Ohtsu et al. (1999) with the same α, β, F_r, and y_t/h parameters (Table 1). The tailwater depth ratio for run I-OA1 was $y_t/h \approx 4.3$ in the range ~4.0 to ~4.6 given by the empirical formulas of Ohtsu et al. (1999) for formation of oscillatory asymmetric SSHJs with $\alpha = 1/3$, $\beta = 5.0$, and $F_r = 3.0$. However, the tailwater depth ratio of 4.3 for run I-OA1 exceeded the minimum tailwater depth $y_t/h \approx 3.8$ calculated from the empirical formula by Rajaratnam and Subramanya (1968) for symmetric SSHJ formation (Equation (3)), implying that no oscillatory behavior should be observed in run I-OA1. Other runs (I-OA5, I-OA6, and I-OA8) that reproduced oscillatory behavior also had tailwater depth ratios exceeding the minimum ratios given by Rajaratnam and Subramanya's (1968) empirical formula. This discrepancy is likely due to the neglect of the expansion ratio α from the formula proposed by Rajaratnam and Subramanya (1968) compared to accounting for α in the simulations and the emprirical formula by Ohtsu et al. (1999).

Besides reproducing oscillatory behavior, the model gave reliable estimates of jump length for oscillatory assymetric SSHJs (Figure 6b). For runs I-OA1 to I-OA8, jump length to head loss ratio L_j/H_l ranged between ~2.8 and ~11.4. Differences from L_j/H_l estimates given by the empirical formula of

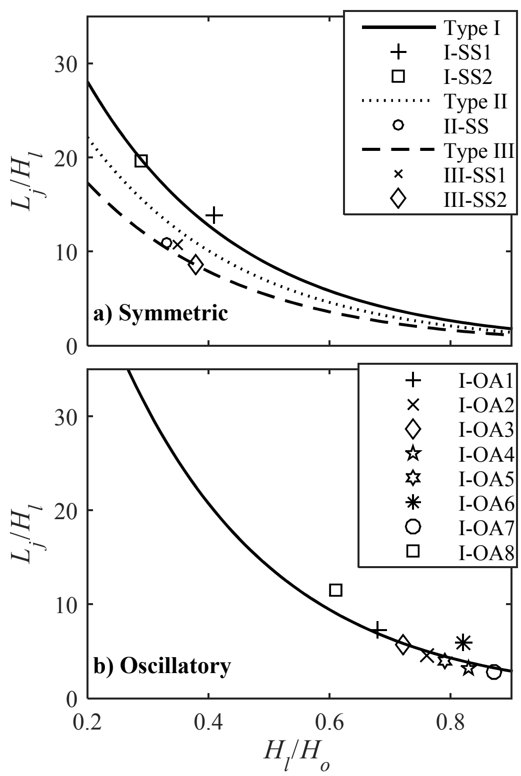

Fig. 6. Ratio of jump length to head loss L_j/H_l versus ratio of head loss to head at inlet H_l/H_o for a) steady symmetric SSHJ and b) oscillatory asymmetric SSHJ. Markers represent results of numerical simulations. Solid lines represent empirical formulas given by Ohtsu et al. (1999). In panel a), the line for type II symmetric SSHJ correspond to $\alpha = 2/3$.

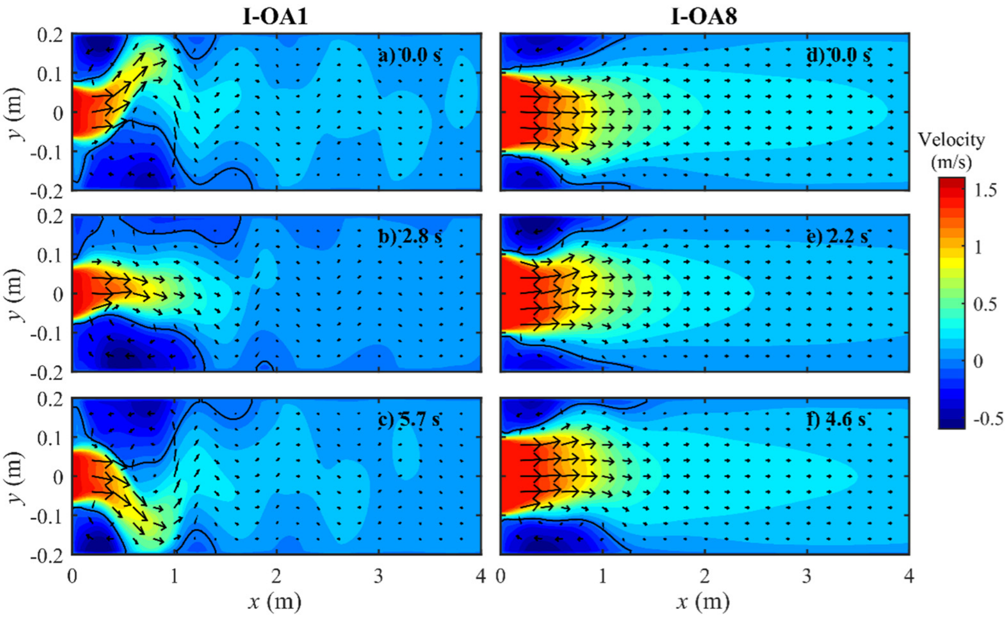

Fig. 7. Distribution of longitudinal velocity over horizontal plane at height $z = 0.01$ m above bed for run I-OA1 (left panels) and run I-OA8 (right panels). Arrows denote horizontal velocity vectors. Run I-OA1 had the parameters $\alpha = 1/3$, $F_r = 3.0$, and $y_t/h = 4.3$. Run I-OA8 had parameters $\alpha = 0.5$, $F_r = 2.3$, and $y_t/h = 3.4$. Both runs had aspect ratio $\beta = 5.0$. Numbers next to panel labels indicate time of snapshot.

Ohtsu et al. (1999) averaged 16%, less than the maximum error of 20% indicated by Ohtsu et al. (1999) for their empirical formula. For runs I-OA1 to I-OA3 which correspond to experiments conducted by Ohtsu et al. (1999), the difference in simulated and empirical jump length was small ranging between 3% and 10%. For other runs, differences were higher ranging between 13% and 45%, implying that the empirical formula by Ohtsu et al. (1999) may need adjustment to give better estimates of jump length for a wider range of SSHJ parameters.

3.2.2 Periodicity and phase shift

For the simulated oscillatory SSHJs, water depth and longitudinal velocity fluctuated periodically with time. An example of these periodic fluctuations is shown in Figure 8 for the results of run I-OA1. For a cross-section at $x/L_j = 0.34$ where maximum fluctuations were observed for run I-OA1, the instantaneous longitudinal velocity at channel centerline 0.02 m above channel bed ranged between 3% and 68% of the inlet velocity (Figure 8a). Near channel walls, instantaneous longitudinal velocity was mostly in the reverse direction and fluctuated in magnitude between –36% and 21% of the inlet velocity (Figure 8a). At the same section $x/L_j = 0.34$, water depth at channel centerline fluctuated between 83% and 90% of tailwater water depth (Figure 8b). Near channel walls, fluctuations in water depth were greater ranging between 82% and 103% of tailwater water depth (Figure 8b).

Water depth fluctuated with identical periods to velocity fluctuations. Spectral analysis revealed that the dominant frequency of velocity and water depth fluctuations at the centerline was 0.18 Hz corresponding to a period of ~5.6 s (Figure 8c). Other smaller spectral peaks at higher frequencies are primarily harmonics of the dominant frequency; these harmonics appear in the power spectra because velocity and water depth fluctuations deviate from pure sinusoidal patterns. At the dominant frequency of ~11.2 s, coherence between water depth and velocity fluctuations was high and approached unity indicating that water depth and velocity fluctuations had similar patterns. The phase shift between the longitudinal velocity and water depth fluctuations was about $-\pi$ indicating that velocity fluctuations were in anti-phase with water depth fluctuations (Figure 8d).

Near channel walls, the period between peak velocities was ~11.2 s, twice the period revealed by spectral analysis for velocity and water depth fluctuations at the channel centreline (Figure 8c). This period of ~11.2 s represents the SSHJ oscillation period; the SSHJ jet crosses the channel centerline twice as the jet deflects from one channel side to the other then back again. For other runs I-OA2 to I-OA8, spectral analysis revealed that dominant jet oscillation frequencies ranged between 0.11 Hz and 0.23 Hz corresponding to periods between about 4 s and 11 s (not shown). Similar to run I-OA1, water depth and velocity fluctuations for runs I-OA2 to I-OA8 were highly coherent at dominant frequencies and were out of phase by quarter of a period.

3.2.3 Factors affecting oscillation period and amplitude

For runs I-OA1 to I-OA8, oscillation frequencies from spectral analysis correspond to Strouhal number S_t ranging from 0.003 to 0.015. For the range of parameters applied in runs I-OA1 to I-OA8, Strouhal number was found to be dependent on the expansion ratio and independent of aspect ratio, Froude number, Reynolds number, and tailwater depth to vent height ratio (Figure 9). The dependence of Strouhal number on expansion ratio α may be represented by a linear relationship with a positive slope; Strouhal number increases with increase in α (Figure 9e).

The amplitude of velocity fluctuations varied with location along channel centerline. The amplitude gradually increased reaching a peak between 18% and 65% of inlet velocity within 20% to 40% of the jump length. The amplitude then steadily diminished dropping to values between ~1% and ~10% of inlet velocity by the downstream end of the jump $(x/L_j > 1)$.

Unlike the frequency of velocity fluctuations, peak normalized amplitudes of velocity fluctuations along channel centerline

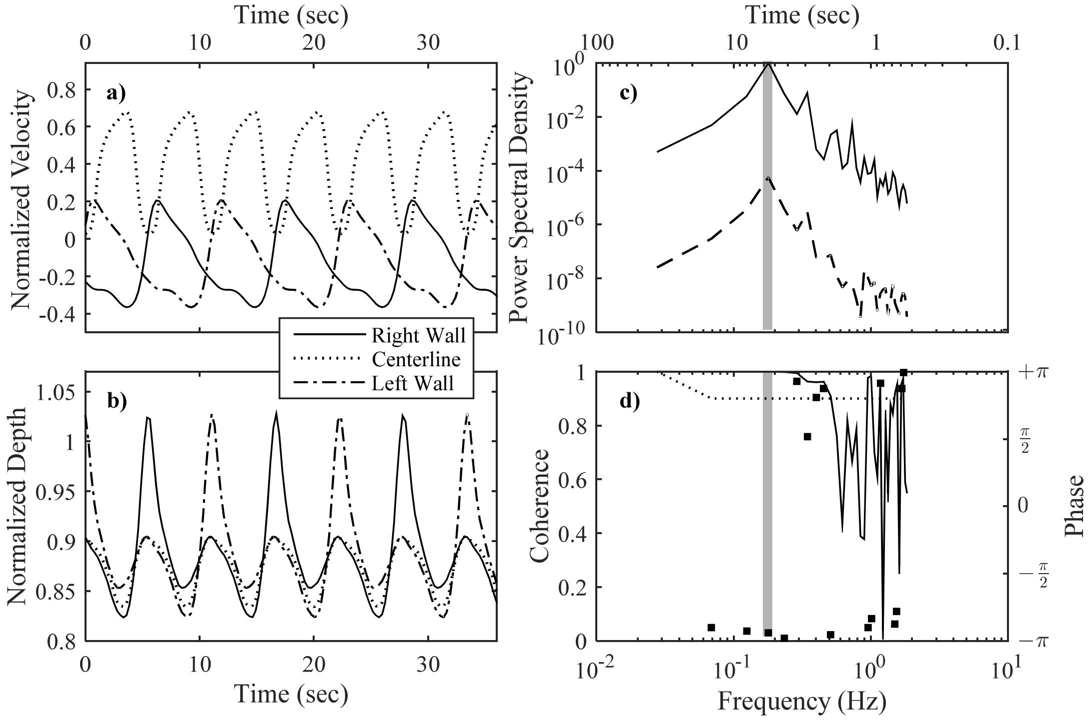

Fig. 8. Simulated normalized a) longitudinal velocity and b) water depth for run I-OA1 at channel centreline and near channel walls at cross-section $x/L_j = 0.34$. Longitudinal velocity is normalized by inlet velocity and water depth is normalized by tailwater depth y_t. c) Power spectra for longitudinal velocity (solid line) and water depth (dashed line) at channel centreline. d) Coherence (solid lines) and phase shift (square markers) between velocity and water depth spectra shown in panel c). Grey shading in panels c) and d) indicate dominant frequency. Dotted line in panel d) gives coherence at the 90% confidence level.

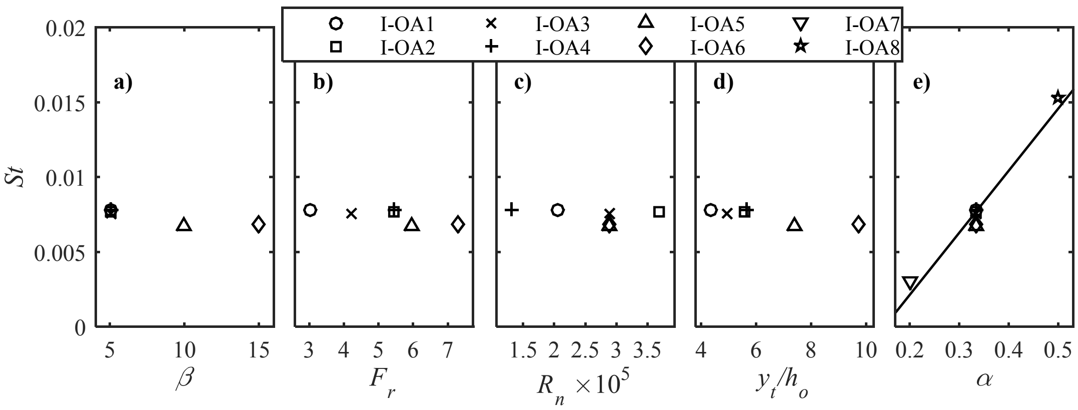

Fig. 9. Strouhal number versus a) aspect ratio, b) Froude number, c) Reynolds number, d) ratio of tailwater depth to vent height, and e) expansion ratio. Solid line in panel e) represents the least squares linear regression relationship $S_t = 0.0415\alpha - 0.0062$.

depended not only on the expansion ratio α, but also on aspect ratio, Froude number, tailwater depth, and Reynolds number. For example, the peak amplitude was 44% of inlet velocity for run I-OA2 with $\alpha = 1/3$, $\beta = 5.0$, $F_r = 5.4$, $y_t/h = 5.6$, and $R_n = 3.7 \times 10^5$. For run I-OA4 with similar parameters except with a smaller $R_n = 1.3 \times 10^5$, the peak amplitude was 51% of inlet velocity greater than in run I-OA2 with higher R_n. A general regression equation that gives peak normalized amplitude as function of α, β, F_n, y_t/h, and R_n could not be reliably deduced without significantly more simulations. However, multivariate regression with standardized coefficients indicated that Froude number and tailwater depth ratio had the greatest effect on the normalized amplitude of velocity fluctuations. Next in effect is expansion and aspect ratios. Reynolds number had the smallest effect on peak normalized amplitude.

3.2.4 Full scale simulation

Similar to runs I-OA1 to I-OA8, oscillatory behavior was observed in model results for run I-OA9 with larger channel dimensions. The period between peak velocities in run I-OA9 was ~35 s giving a frequency of 0.029 Hz. The corresponding Strouhal number was 0.0078, identical to the value calculated from the linear regression relationship deduced earlier. The consistency in oscillatory behaviour simulated for small and large scale domains indicates that scale effects on model results are insignificant. This conclusion is also supported by good reproduction of jump length for simulations in both small and large domains. For run I-OA9, the calculated jump length from the simulation results was ~17.6 m, only 16% higher than a length of 14.8 m obtained from the equation by Ohtsu et al. (1999).

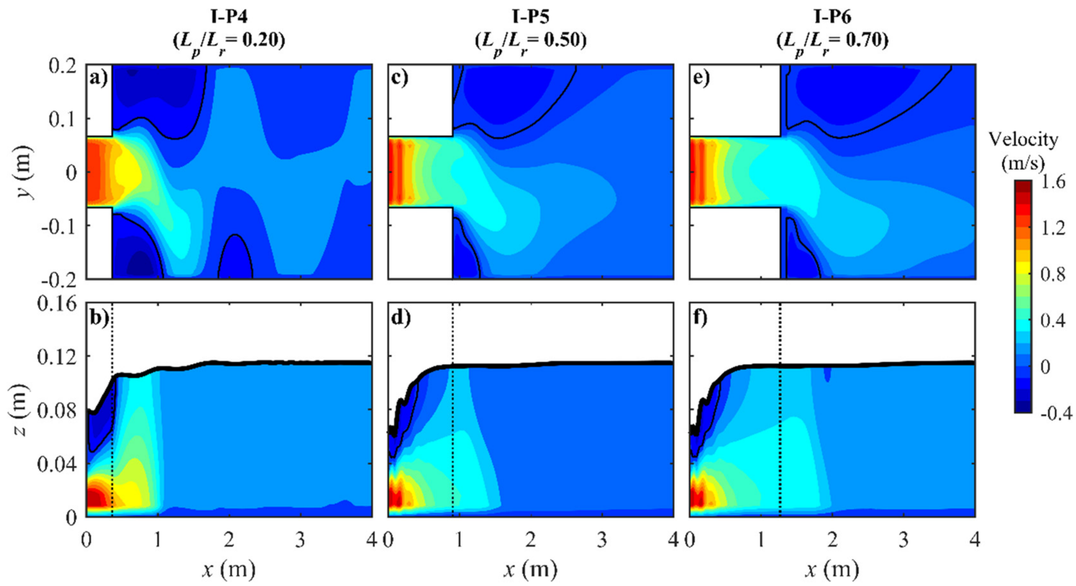

Fig. 10. Distribution of longitudinal velocity over horizontal plane at height $z = 0.02$ m above channel bed (upper panels) and along channel centreline (lower panels) for run I-P4 (a, b), run I-P5 (c, d), and run I-P6 (e, f). All three runs had $\alpha = 1/3$, $\beta = 5.0$, and $F_r = 3.0$.

3.3 Pier effect on oscillatory SSHJ

The existence of piers downstream of vents altered the structure of oscillatory SSHJs. Velocity and water depth became symmetrically distributed in between the piers but continued to be asymmetrically distributed downstream of the piers (Figure 10). When the ratio of pier length to jump length L_p/L_j was relatively small ($\lesssim 0.2$), the SSHJ jet downstream of the piers exhibited oscillatory deflections similar to those simulated in run I-OA1 without piers (Figure 10a, b). For piers with $L_p/L_j \gtrsim 0.5$, the SSHJ jet steadily deflected towards one of the channel walls with negligible oscillatory behavior (Figure 10c–f).

With increase in pier length, the simulated depth immediately downstream of the vent decreased as observed for submerged transitional jumps (T-jumps) (Smith 1989). The flow out of the vent became less submerged approaching the flow pattern of free hydraulic jumps. Runs with pier length ratios $L_p/L_j \geq 0.5$ reproduced free surface fluctuations characteristic of free jump rollers (Figure 10d, f). These free surface fluctuations occurred between the piers with corresponding fluctuations in longitudinal velocity but without the cross-channel jet deflections characteristic of oscillatory SSHJ (Figure 10c–f). Spectral analysis of the simulated fluctuations indicated a dominant frequency of 1.4 Hz consistent with the value obtained from the empirical formula by Mok et al. (2013) which relates the frequency of free-surface fluctuations to inlet velocity and roller length of free jump, $f = U/2L_j$. This agreement between simulated and observed frequency indicates that the model satisfactorily reproduces the transition of SSHJ to free jump.

4 CONCLUSIONS

Submerged spatial hydraulic jumps (SSHJs) below abrupt symmetrical expansions have been studied numerically for different values of several parameters including expansion ratio, aspect ratio, Froude number, and ratio of tailwater depth to vent height. The applied numerical model indicated that SSHJs had three-dimensional patterns that would not be accurately simulated with two-dimensional numerical models previously employed to examine classical hydraulics jumps.

The three-dimensional numerical model in this study correctly simulated all types of SSHJ. In particular, the model was capable of simulating oscillatory SSHJ although symmetric initial and boundary conditions were imposed. Simulated water depth and longitudinal velocity in oscillatory SSHJ were found to be in anti-phase indicating a feedback mechanism between static pressure and velocity. The Strouhal number characterizing the frequency of jet deflections of oscillatory SSHJ was found to be dependent on only the expansion ratio. The existence of piers downstream of vents tended to eliminate asymmetric flow between the piers but did not alter the symmetry of flow downstream of the piers. However, oscillatory jet deflections diminished with increase in pier length. For pier lengths 50% or more of the jump length, the SSHJ jet downstream of the piers became steadily deflected towards one of the channel walls.

REFERENCES

Akoz, M.S., Kirkgoz, M.S., Oner, A.A., 2009. Experimental and numerical modeling of a sluice gate flow. Journal of Hydraulic Research, 47, 2, 167–176.

Bijankhan, M., Kouchakzadeh, S., 2015. The hydraulics of parallel sluice gates under low flow delivery condition. Flow Measurement and Instrumentation, 41, 140–148.

Bremen, R., Hager, W.H., 1993. T-jump in abruptly expanding channel. Journal of Hydraulic research, 31, 1, 61–78.

Demirel, E., 2015. Measured and simulated flow downstream of the submerged sluice gate. Water and Environment Journal, 29, 3, 446–455.

Gumus, V., Simsek, O., Soydan, N.G., Akoz, M.S., Kirkgoz, M.S., 2016. Numerical modeling of submerged hydraulic jump from a sluice gate. Journal of Irrigation and Drainage Engineering, 142, 1. DOI: 10.1061/(asce)ir.1943-4774.0000948

Hager, W.H., 1992. Energy Dissipators and Hydraulic Jump. Springer Science & Business Media, Springer, Dordrecht. DOI: 10.1007/978-94-015-8048-9

Helmi, A.M., Essawy, H.T., Wagdy, A., 2019. Three-dimensional numerical study of stacked drop manholes. Journal of Irrigation and Drainage Engineering, 145, 9. DOI: 10.1061/(ASCE)IR.1943-4774.0001414

Hirt, C.W., Nichols, B.D., 1981. Volume of fluid (VOF) method for the dynamics of free boundaries. Journal of Computational Physics, 39, 1, 201–225.

Javan, M., Eghbalzadeh, A., 2013. 2D numerical simulation of submerged hydraulic jumps. Applied Mathematical Modelling, 37, 10–11, 6661–6669.

Jesudhas, V., Roussinova, V., Balachandar, R., Barron, R., 2017. Submerged hydraulic jump study using DES. Journal of Hydraulic Engineering, 143, 3, Article number: 04016091.

Jesudhas, V., Balachandar, R., Roussinova, V., Barron, R., 2018. Turbulence characteristics of classical hydraulic jump using DES. Journal of Hydraulic Engineering, 144, 6. DOI: 10.1061/(ASCE)HY.1943-7900.0001427.

Jesudhas, V., Balachandar, R., Bolisetti, T., 2020a. Numerical study of a symmetric submerged spatial hydraulic jump. Journal of Hydraulic Research, 58, 2, 335–349.

Jesudhas, V., Balachandar, R., Wang, H., Murzyn, F., 2020b. Modelling hydraulic jumps: IDDES versus experiments. Environmental Fluid Mechanics, 20, 2, 393–413.

Long, D., Steffler, P.M., Rajaratnam, N., 1991. A numerical study of submerged hydraulic jumps. Journal of Hydraulic Research, 29, 3, 293–308.

Ma, F., Hou. Y., Prinos, P., 2001. Numerical calculation of submerged hydraulic jumps. Journal of Hydraulic Research, 39, 5, 493–503.

Mok, K.M., Yuen, K.V., Cheong, K.H., Hoi, K.I., 2013. A search for the dominant free surface-fluctuation frequency downstream of the oscillating hydraulic jump with the Bayesian spectral density approach. Physica Scripta, 2013, T155. DOI: 10.1088/0031-8949/2013/T155/014007

Nguyen, V.T., Nestmann, F., 2004. Applications of CFD in hydraulics and river engineering. International Journal of Computational Fluid Dynamics, 18, 2, 165–174.

Ohtsu, I., Yasuda, Y., Ishikawa, M., 1999. Submerged hydraulic jumps below abrupt expansions. Journal of Hydraulic Engineering, 125, 5, 492–499.

Qingchao, L., Drewes, U., 1994. Turbulence characteristics in free and forced hydraulic jumps. Journal of Hydraulic Research, 32, 6, 877–898.

Rajaratnam, N., Subramanya, K., 1968. Hydraulic jumps below abrupt symmetrical expansions. Journal of the Hydraulics Division, 94, 2, 481–504.

Roache, P.J., 1998. Verification and Validation in Computational Science and Engineering. Hermosa, 446 p.

Shaari, K.Z.K., Awang, M., 2015. Engineering Applications of Computational Fluid Dynamics. Springer.

Smith, C.D., 1989. The submerged hydraulic jump in an abrupt lateral expansion. Journal of Hydraulic Research, 27, 2, 257–266.

Zare, H.K., Baddour, R.E., 2007. Three-dimensional study of spatial submerged hydraulic jump. Canadian Journal of Civil Engineering, 34, 9, 1140–1148.

Zare, H.K., Baddour, R.E., 2007. Three-dimensional study of spatial submerged hydraulic jump. Canadian Journal of Civil Engineering, 34, 9, 1140–1148.

NOMENCLATURE

b - vent width (m)
B - channel width (m)
F_r - Froude number (–)
f_v - volume of fluid
g - gravitational acceleration (m s^{-2})
h - vent height (m)
H_l - head loss (m)
H_o - total head at vent outlet (m)
L_p - pier length (m)
L_r - jump roller length (m)
R_e - Reynolds number (–)
S_t - Strouhal number (–)
U - velocity through inlet vent (m s^{-1})
u_o - observed velocity (m s^{-1})
$\overline{u_o}$ - average velocity (m s^{-1})
u_s - simulated velocity (m s^{-1})
y_t - tailwater depth (m)
Y_t - tailwater depth to vent height ratio (–)
α - expansion ratio (–)
β - vent aspect ratio (–)
ν - kinematic viscosity of water (m^2 s^{-1})

Received 12 February 2019
Accepted 28 April 2020